A Virtual Admittance-Based State Observer Design for Enhanced Dynamic Synchronization Performance of Virtual Synchronous Generator

Dongren Dai, Jinghua Li, *Senior Member, IEEE*, Fei Lan, and Wei Tian, *Member, IEEE*

***Abstract*—The virtual resistor (VR) has positive effects on the small-signal stability of the virtual synchronous generator (VSG), but decreases the dynamic-state synchronization performance. To solve that conflict, a virtual admittance (VA)-based state observer (VABOB) is designed. First, the small-signal model of the VSG is analyzed, and it is found that the extra VR is only needed at 0 Hz to suppress the synchronous frequency resonance (SFR). The extra resistor at the synchronous frequency (SF) will decrease the dynamic response performance. Second, a state equation is designed for the accurate estimation of the SF component, and the VA without VR is designed as the output equation. Then, the state observer is deduced based on these equations. Third, the analysis of the grid voltage and frequency deviation shows the robustness of the VABOB. Furthermore, the selection principle for the observer gain is also analyzed. Simulations and experiments verify the effectiveness of the VABOB in SFR suppression and dynamic performance enhancement by reducing the R/X. The VABOB can reduce the maximum by 0.39 p.u. power overshoot when the grid voltage is sagged by 0.1 p.u., as compared to the VR-based method with $R/X = 0.19$. By 0.55 p.u. reactive power overshoot reduction when power given is increased from 0 to 1 p.u., as compared to the VR-based method with $R/X = 0.83$.**

***Index Terms*—Dynamic response performance, small-signal model, state observer, virtual admittance, virtual synchronous generator (VSG).**

I. Introduction

With the increase of new energy penetration rate, grid-forming (GFM) inverters have attracted much attention due to their grid-friendly features, such as voltage-supporting ability, frequency response-ability, and weak grid synchronization ability [1], [2], [3]. The GFM inverters are required to take part in the frequency or voltage regulation of the grid, as compared to the interaction-free grid-following (GFL) inverters. In other words, the grid frequency or grid voltage fluctuation can be compensated by the GFM inverters automatically.

Received 23 July 2025; revised 29 November 2025; accepted 27 December 2025. Date of publication 5 January 2026; date of current version 20 March 2026. This work was supported by the National Natural Science Foundation of China under Grant 52367004. Recommended for publication by Associate Editor M. Su. *(Corresponding author: Jinghua Li.)*

The authors are with School of Electrical Engineering, Guangxi University, Nanning 530004, China (e-mail: 2312401002@st.gxu.edu.cn; lijinghua@gxu.edu.cn; lanfei88@gxu.edu.cn; yeyu@gxu.edu.cn).

Color versions of one or more figures in this article are available at https://doi.org/10.1109/TPEL.2026.3650955.

Digital Object Identifier 10.1109/TPEL.2026.3650955

The virtual synchronous generator (VSG) is a typical grid-forming strategy, which is proposed to realize the external characteristics of the synchronous generator based on the PWM inverters [4]. Unlike the phase-locked loop (PLL)-based GFL inverters, the VSG does not rely on the PLL to synchronize with the grid; it uses the power synchronous pattern [5]. However, the VSG suffers from small-signal stability problems, which may cause the VSG to be off the grid or, worse, transmit this instability to the grid. Therefore, how to improve the VSG's small-signal stability is a meaningful topic [6]. The small-signal stability is the power synchronization stability under the small disturbances around the steady-state working point. This underdamped-caused instability is usually presented as periodic synchronization power oscillations, thus defined as synchronous frequency resonance (SFR) [7], [8]. Besides, the low-frequency oscillations (LFO) [9], [10] and the subsynchronous oscillations [11] are also periodic.

Therefore, researchers have proposed different damping methods to suppress the SFR. First of all, when the dynamics of grid impedance are considered, two conjugate poles occur in the open-loop small-signal model of VSG. These two poles result in a resonance peak and 180° phase lag around the synchronous frequency (SF). The direct way to eliminate the SFR is by tuning the two poles; the virtual resistor (VR) is often used to add a negative real root for the poles [12]. Further, if the virtual inductor is considered, the VR has evolved into the virtual impedance (VI), and the general control structures for voltage-source converters and current-source converters were reviewed in [13]. One characteristic of VI is that the virtual inductor may introduce the differential terms sL. Therefore, the quasi-stationary inductor model $j\omega L$ is often used to avoid the differential operation [14], [15]. Some researchers have used the virtual admittance (VA) model for VSG to get a smoother reference [16], [17], [18], which transforms the voltage into the current by multiplying the $1/(R+sL)$. This can be realized by an integrator and feedback [19].

However, researchers revealed that the VR has negative effects on the VSG's and dynamic stability, as it increases the R/X ratio [20]. When the grid voltage is dropped, the negative influence on the transient stability is also reported [21]. Therefore, to minimize the VR, the adaptive VR method and adaptive damping coefficient method are proposed to find the balance between the SFR elimination and transient performance [22]. A transient

VR method is also proposed to enhance the transient stability in this dynamic state [23]. Considering the overall effect of VR, extra auxiliary branches, based on the feedforward decoupling or the extended state observer, are proposed to eliminate the SFR and broaden the control bandwidth [24], [25]. Furthermore, a geometrical approach method is proposed to show the stability boundary intuitively and achieve robust synchronization stability [26].

Besides, an advanced disturbance observer-based VI (DOB-VI) method is proposed by the researchers [27]. The DOB-VI strategy is achieved by utilizing a complete impedance model without the approximation, leading to an accurate emulation of VI. It improves the VSG's stability by rejecting the unmodeled disturbances. However, the VR-based stability against the SFR and the transient SFR are and need to be studied [28], [29], [30], where the transient SFR is the decreasing SFR caused by the voltage sag, and is overlaid on the VSG's convergence path.

In review of the above SFR challenges, VR-based methods can mitigate the SFR amplitude by tuning the poles at the pole frequency (dc component). However, it deteriorated the dynamic-state performance by increasing the *R*/*X* ratio at the SF component. From the perspective of solving the above conflict, the VA-based state observer (VABOB) is studied. The VABOB is designed to represent 0 VR at the SF component and the extra VR at the dc component. Thus, the VABOB can eliminate the SFR by the extra VR at the dc component, and increase the dynamic performance by decreasing the *R*/*X* ratio at the SF component. In conclusion, the main points of the article are listed as follows.

1) A virtual admittance-based state observer is proposed, which effectively suppresses the SFR and enhances the dynamic-state synchronization performance.
2) The stability of the VABOB against the grid frequency drop and voltage sag is analyzed, and its improvements to the VSG are proved through the *P*/ω model and the phase portrait.
3) Furthermore, the observer parameter selection principle is proposed, toward improving the SFR suppression effect and dynamic performance.

The structure of this article is organized as follows: Section II introduces the VA-based VSG and the small-signal model. The VABOB is proposed in Section III. The corresponding steady-state and dynamic-state errors are also discussed in this section. In Section IV, the active power control loop (APCL) stability is studied through the *P*/ω model, and represented by the *R*/*X* ratio. The transient SFR is derived through the time-domain solutions. The phase portrait verifies the VABOB against the transient SFR. The simulations and comparative experimental studies are listed in Section V, which verifies the effectiveness of the VABOB in eliminating SFR and improving the dynamic-state performance. Finally, Section VI summarizes the work of the article.

II. Small-Signal Modeling and Damping Method

In this section, the conventional VA-based VSG is described, and the small-signal model is established. Furthermore, the steady-state SFR is also derived and found to be caused by the lack of damping at the pole frequency.

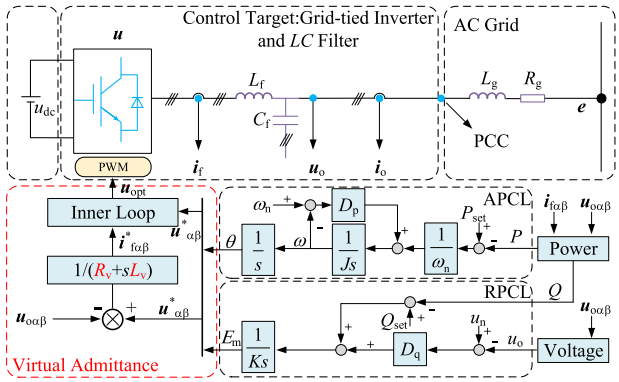

Fig. 1. Block diagram of the VSG control system.

A. Conventional Virtual Admittance-Based VSG

The VSG control system is shown in Fig. 1, where u_{dc} is the dc-link voltage, and $\boldsymbol{e}$ is the grid voltage. The R_{g} and L_{g} are the grid resistance and grid inductance. The L_{f} and C_{f} are the filter inductance and filter capacitance. $\boldsymbol{u}_{\mathrm{o}}$ is the capacitor voltage (PCC voltage), $\boldsymbol{i}_{\mathrm{f}}$ and $\boldsymbol{i}_{\mathrm{o}}$ are the inverter's output and grid currents, respectively. L_{v} and R_{v} are the virtual inductance and resistance values. The subscript α, β means the projection on the corresponding axis.

The APCL and the reactive power control loop (RPCL) are modeled as follows:

$$\begin{cases} \frac{P_{\mathrm{set}}}{\omega} - \frac{P_{\mathrm{e}}}{\omega} + D_{\mathrm{p}}(\omega_{\mathrm{n}} - \omega) = J\frac{\mathrm{d}\omega}{\mathrm{d}t} \\ \theta = \int \omega \mathrm{d}t \end{cases} \tag{1}$$

where J and D_{p} are the rotational inertia and damping coefficient, respectively; ω_{n} and ω are the rated and real angular speed of VSG, respectively; P_{set} and P_{e} are the mechanical and electromagnetic power, respectively

$$Q_{\mathrm{set}} - Q_{\mathrm{e}} + D_{\mathrm{q}}(u_{\mathrm{n}} - u_{\mathrm{o}}) = K\frac{\mathrm{d}E_{\mathrm{m}}}{\mathrm{d}t} \tag{2}$$

where K and D_{q} are the integrator gain and voltage-drooping coefficient; the u_{n} and u_{o} are the rated voltage and real voltage at PCC, respectively, and E_{m} is the grid voltage amplitude.

Now that the amplitude E_{m} and the phase θ are known, the reference voltage for the inner control loop can be generated:

$$u^*_{\alpha\beta} = E_{\mathrm{m}}\left[\cos(\theta), \cos\left(\theta - \frac{\pi}{2}\right)\right]^{\mathrm{T}}. \tag{3}$$

For the VA-based method, the reference current is further deduced as follows:

$$i^*_{\mathrm{f}\alpha\beta} = \frac{u^*_{\alpha\beta} - u_{\mathrm{o}\alpha\beta}}{(sL_{\mathrm{v}} + R_{\mathrm{v}})}. \tag{4}$$

B. Small-Signal Model

To study the stability of the VSG system, the small-signal model is shown in Fig. 2 first. It contains two parts, the VSG part and the power part. In the VSG part, APCL and RPCL transfer functions are $G_P(s)$ and $G_Q(s)$, respectively. The power part transfer functions are $\boldsymbol{K}(s) = [\boldsymbol{K}_1(s), \boldsymbol{K}_2(s), \boldsymbol{K}_3(s), \boldsymbol{K}_4(s)]^{\mathrm{T}}$.

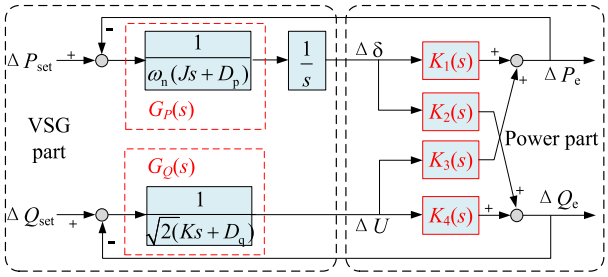

Fig. 2. Small-signal transfer diagram of VSG.

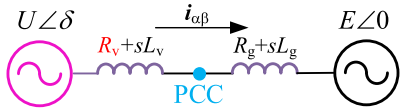

Fig. 3. Steady-state VSG model.

The VSG part is intuitively shown in Fig. 2. The ΔP and ΔQ are the functions of ΔU and $\Delta\delta$, which are denoted as $\boldsymbol{K}(s)$. To figure out the transfer functions $\boldsymbol{K}(s)$, the VSG and grid are linearized at the working points $U\angle\delta$ and $E\angle 0$, respectively, as shown in Fig. 3. $\boldsymbol{i}_{\alpha\beta}$ is the current from the VSG to the grid.

First, the active and reactive power of the VSG is defined as follows:

$$\begin{bmatrix} P \\ Q \end{bmatrix} = \frac{3}{2}\begin{bmatrix} u_\alpha & u_\beta \\ u_\beta & -u_\alpha \end{bmatrix}\begin{bmatrix} i_\alpha \\ i_\beta \end{bmatrix}. \tag{5}$$

The small deviations and the steady-state working points are prefixed by Δ and denoted by subscript "0," respectively

$$\begin{aligned} P &= P_0 + \Delta P \\ Q &= Q_0 + \Delta Q \\ u_\alpha &= u_{\alpha 0} + \Delta u_\alpha \\ u_\beta &= u_{\beta 0} + \Delta u_\beta \\ i_\alpha &= i_{\alpha 0} + \Delta i_\alpha \\ i_\beta &= i_{\beta 0} + \Delta i_\beta. \end{aligned} \tag{6}$$

Thus, (5) can be expressed as follows:

$$\begin{bmatrix} P_0+\Delta P \\ Q_0+\Delta Q \end{bmatrix} = \frac{3}{2}\begin{bmatrix} u_{\alpha 0}+\Delta u_\alpha & u_{\beta 0}+\Delta u_\beta \\ u_{\beta 0}+\Delta u_\beta & -(u_{\alpha 0}+\Delta u_\alpha) \end{bmatrix}\begin{bmatrix} i_{\alpha 0}+\Delta i_\alpha \\ i_{\beta 0}+\Delta i_\beta \end{bmatrix}. \tag{7}$$

Due to the active power P_0 and the reactive power Q_0 [following the steady-state power (5)], and the second-order small deviations ($\Delta\boldsymbol{u}_\alpha\Delta\boldsymbol{i}_\alpha$, $\Delta\boldsymbol{u}_\beta\Delta\boldsymbol{i}_\beta$, $\Delta\boldsymbol{u}_\alpha\Delta\boldsymbol{i}_\beta$, and $\Delta\boldsymbol{u}_\beta\Delta\boldsymbol{i}_\alpha$) are ignored, (7) can be further deduced as follows:

$$\begin{bmatrix} \Delta P \\ \Delta Q \end{bmatrix} = M_{\alpha\beta}(t)\begin{bmatrix} \Delta u_\alpha & \Delta u_\beta & \Delta i_\alpha & \Delta i_\beta \end{bmatrix}^{\mathrm{T}}$$

$$M_{\alpha\beta}(t) = \frac{3}{2}\begin{bmatrix} i_{\alpha 0} & i_{\beta 0} & u_{\alpha 0} & u_{\beta 0} \\ -i_{\beta 0} & i_{\alpha 0} & u_{\beta 0} & -u_{\alpha 0} \end{bmatrix}. \tag{8}$$

In the stationary coordinate system, the steady-state matrix $M_{\alpha\beta}(t)$ can be deduced by solving the following equation:

$$\begin{bmatrix} u_{\alpha 0} \\ u_{\beta 0} \end{bmatrix} = \sqrt{2}\begin{bmatrix} U_0 cos(\delta_0+\theta) \\ U_0 sin(\delta_0+\theta) \end{bmatrix}$$

$$i_{\alpha 0} + j i_{\beta 0} = \frac{(u_{\alpha 0}-e_{\alpha 0})+j(u_{\beta 0}-e_{\beta 0})}{R+jX}. \tag{9}$$

Another part is small-signal deviations, the $\Delta\boldsymbol{u}_{\alpha\beta}$ is deduced by linearizing the steady-state working point

$$\begin{bmatrix} \Delta u_\alpha \\ \Delta u_\beta \end{bmatrix} = \begin{bmatrix} \frac{\partial u_\alpha}{\partial\delta} & \frac{\partial u_\alpha}{\partial U} \\ \frac{\partial u_\beta}{\partial\delta} & \frac{\partial u_\beta}{\partial U} \end{bmatrix} = H_{\alpha\beta}(t)\begin{bmatrix} \Delta\delta \\ \Delta U \end{bmatrix}$$

$$H_{\alpha\beta}(t) = \sqrt{2}\begin{bmatrix} -U_0\sin(\delta_0+\theta) & \cos(\delta_0+\theta) \\ U_0\cos(\delta_0+\theta) & \sin(\delta_0+\theta) \end{bmatrix}. \tag{10}$$

The relationship between the $\Delta\boldsymbol{i}_{\alpha\beta}$ and $\Delta\boldsymbol{u}_{\alpha\beta}$ is as follows:

$$\begin{bmatrix} \Delta i_\alpha \\ \Delta i_\beta \end{bmatrix} = N_{\alpha\beta}(s)\begin{bmatrix} \Delta u_\alpha \\ \Delta u_\beta \end{bmatrix}$$

$$N_{\alpha\beta}(s) = \frac{I}{R+sL},\ s = -R+j0 \tag{11}$$

where $R = R_v + R_g$, $L = L_v + L_g$, and I is the 2x2 unit matrix.

According to the expression of $N_{\alpha\beta}(s)$, the pole is $s = -R+j0$. When R is small, the current $\Delta\boldsymbol{i}_{\alpha\beta}$ has a large gain on the dc component. Due to the voltage being a synchronous sine wave, synchronous power oscillation occurs. As the oscillation is caused by the low value of R_g, the R_v is useful for suppression.

The $\boldsymbol{K}_{\alpha\beta}(s)$ is deduced by substituting (9)–(11) into (8):

$$K_{\alpha\beta}(s) = M_{\alpha\beta}(t)\begin{bmatrix} I \\ N_{\alpha\beta}(s) \end{bmatrix} H_{\alpha\beta}(t). \tag{12}$$

As the main power response is at the SF, the separate $\boldsymbol{K}_{\alpha\beta}(s)$ can be deduced by substituting $s = j\omega_n$ into $N_{\alpha\beta}(s)$:

$$\begin{aligned} K_1(s) &= \frac{3}{2}\frac{1}{R^2+X^2}(RU_0E\sin\delta_0 + XU_0E\cos\delta_0) \\ K_2(s) &= \frac{3}{2}\frac{1}{R^2+X^2}(R(2U_0 - E\cos\delta_0) + XE\sin\delta_0) \\ K_3(s) &= \frac{3}{2}\frac{1}{R^2+X^2}(XU_0E\sin\delta_0 - RU_0E\cos\delta_0) \\ K_4(s) &= \frac{3}{2}\frac{1}{R^2+X^2}(X(2U_0 - E\cos\delta_0) - RE\sin\delta_0). \end{aligned} \tag{13}$$

III. VABOB Design and Analysis

The VABOB is designed in this section. First, the state equation and the output equation are designed based on the assumption that $s = j\omega_n$. Then, the state observer is deduced based on the equations. Furthermore, the convergence of the state observer is proved. Then, the steady-state performance at the dc and the SF, the stability against grid voltage and frequency deviation are analyzed.

A. Virtual Admittance Design

At the SF, the differential operator s is equal to $j\omega_n$, thus, the VA method is designed as follows:

$$sL_v i^*_{f\alpha\beta} = j\omega_n L_v i^*_{f\alpha\beta}$$
$$su_{o\alpha\beta} = j\omega_n u_{o\alpha\beta}. \tag{14}$$

Therefore, the state equation is deduced according to (14)

$$\frac{d\boldsymbol{x}}{dt} = \boldsymbol{A}\boldsymbol{x} \tag{15}$$

where

$$\boldsymbol{x} = \begin{bmatrix} \boldsymbol{i}^*_{f\alpha\beta} \\ \boldsymbol{u}_{o\alpha\beta} \end{bmatrix}$$
$$\boldsymbol{A} = \begin{bmatrix} j\omega_n & 0 \\ 0 & j\omega_n \end{bmatrix}. \tag{16}$$

Feedback is needed to correct the errors in the state equation caused by the disturbance. According to (14), it is also assumed that the $s = j\omega_n$. And R_v is reduced to 0 to ensure the dynamic response performance:

$$u^*_{\alpha\beta} - u_{o\alpha\beta} = j\omega_n L_v i^*_{f\alpha\beta}. \tag{17}$$

Therefore, the output equation is derived according to (17):

$$y = \begin{bmatrix} u^*_{\alpha\beta} \\ u_{o\alpha\beta} \end{bmatrix} = \begin{bmatrix} j\omega_n L_v & 1 \\ 0 & 1 \end{bmatrix} x = Cx. \tag{18}$$

B. State Observer Design

Inspired by studies [31] and [32], to achieve an accurate estimation at SF, the state observer is designed based on the state (15) and output (18):

$$\frac{d\hat{\boldsymbol{x}}}{dt} = \boldsymbol{A}\hat{\boldsymbol{x}} + \boldsymbol{L}(\boldsymbol{y} - \boldsymbol{C}\hat{\boldsymbol{x}}) \tag{19}$$

where superscript $\hat{}$ denotes the observed value, and $\boldsymbol{L}$ is the feedback gain matrix.

Subtracting (19) from (15), the observer error is as follows:

$$\frac{d\Delta x}{dt} = (A - LC)\,\Delta x$$
$$\Delta x = x - \hat{x}. \tag{20}$$

The eigenvalues of (20) must be less than zero to make the observer converge; one of the solutions is as follows:

$$\boldsymbol{L} = (\boldsymbol{A} + k\boldsymbol{I})\,\boldsymbol{C}^{-1} \tag{21}$$

where k is the only parameter that should be designed.

Therefore, we obtain $\boldsymbol{A}_1 = \boldsymbol{A} - \boldsymbol{LC} = -k\,\boldsymbol{I}$. The eigenvalue is as follows:

$$\lambda = -k. \tag{22}$$

When $k > 0$, the observer converges.

The corresponding implementation is shown in Fig. 4. The state observer needs the output voltage $\boldsymbol{u}_{o\alpha\beta}$ and the reference voltage $\boldsymbol{u}^*_{\alpha\beta}$ to estimate the state variables. As the VA method is integrated in the observer, after the estimation, the state variables $\hat{\boldsymbol{u}}_{o\alpha\beta}$ and $\hat{\boldsymbol{i}}^*_{f\alpha\beta}$ can be used for the current controller

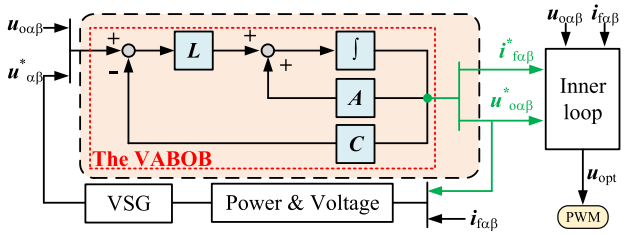

Fig. 4. Implementation of the VABOB.

directly. Moreover, the $\hat{\boldsymbol{u}}_{o\alpha\beta}$ can be used for power and voltage calculation to prefilter the inputs.

C. Steady-State Error Analysis

To analyze the steady-state error of the VABOB, the transfer function is studied first. Substituting (21) into (19), the function between real $\boldsymbol{x}$ and observed $\hat{\boldsymbol{x}}$ is derived first

$$\hat{x} = G_{OB}(s)\,x$$
$$G_{OB}(s) = \frac{j\omega_n + k}{s + k}. \tag{23}$$

This is, the observer is a low-pass filter (LPF), and the parameter k is the cut-off frequency. Therefore, the VABOB can filter the high-order harmonics with lower k, thus, the maximum k is limited to 1/10 of the control frequency f_s.

Next, the system's admittance under the VABOB will be discussed. First, expand the first row of (23), and due to the $\boldsymbol{x} = \boldsymbol{C}^{-1}\,\boldsymbol{y}$, the observed current equals to

$$\hat{i}^*_{f\alpha\beta} = G_{OB}(s)\,\frac{u^*_{\alpha\beta} - u_{o\alpha\beta}}{j\omega_n L_v}. \tag{24}$$

It indicates that the impedance from the VSG to the PCC is $j\omega_n R_v$. The impedance from the PCC to the grid, being $R_g + sL_g$, therefore, (24) equals

$$\hat{i}^*_{f\alpha\beta} = G_{OB}(s)\,\frac{1}{(R_g + sL_g + j\omega_n L_v)}\left(u^*_{\alpha\beta} - e_{\alpha\beta}\right). \tag{25}$$

A simpler understanding is that the impedance is scaled by the $\boldsymbol{G}_{OB}(s)$:

$$Z' = \frac{(R_g + sL_g + j\omega_n L_v)}{\boldsymbol{G}_{OB}(s)} \tag{26}$$

where Z' is the impedance under the VABOB.

If $s = j0$ is substituted into (26), the dc resistor R_{dc} can be expressed as follows:

$$R_{dc} = k\left[\frac{kR_g + \omega_n^2 L_v}{k^2 + \omega_n^2} + j\omega_n \frac{kL_v - R_g}{k^2 + \omega_n^2}\right] \tag{27}$$

where the subscript dc means the dc component.

The R_{dc} provided by the VABOB contains the real part and the imaginary part. This can be explained in Fig. 5, as the dc voltage also contains the real part and the imaginary part, the current response is with a phase shift and an amplitude.

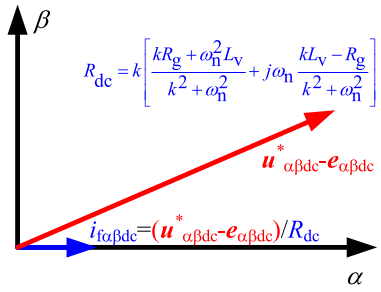

Fig. 5. Effect of the R_{dc}.

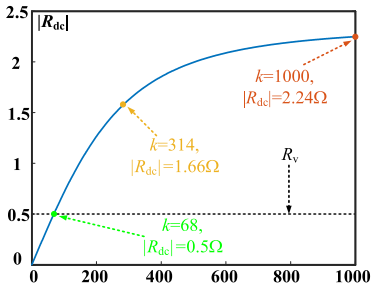

Fig. 6. Relationship between $|R_{dc}|$ and k.

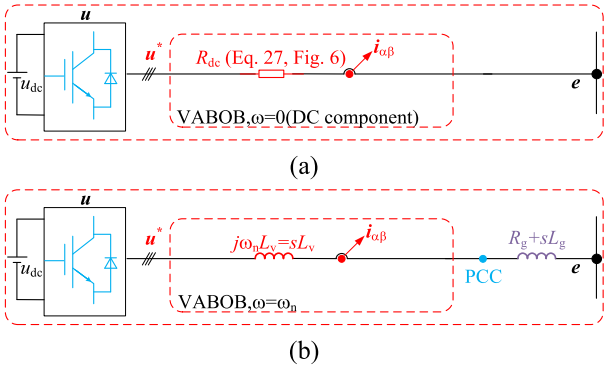

Fig. 7. Equivalent circuit under the VABOB. (a) At DC. (b) At the SF.

As described in the small-signal model before, the SFR is an underdamped dc component multiplied by the synchronous voltage. Therefore, it is more dominated by the amplitude response. To get the amplitude response, take the modulus of R_{dc} in (27), the Fig. 6 is obtained. The k is increased from 0 to 1000. When k is 68, the $|R_{dc}|$ is equal to the selected $R_v = 0.5\ \Omega$. Then, when k is 314 and 1000, the $|R_{dc}|$ is 1.66 and 2.24 Ω, respectively. Thus, the VABOB can damp the SFR.

If the $s = j\omega_n$ is substituted in (26), the observer's estimation for the SF component is:

$$\hat{x}\left(s=j\omega_n\right)=x\left(s=j\omega_n\right)$$
$$G_{OB}\left(s=j\omega_n\right)=1. \tag{28}$$

Concluding the above impedance discussion of dc and the SF component, the equivalent circuit of the VSG under the VABOB is shown in Fig. 7. At the dc component, only the dc resistor R_{dc} is valid, and the R_{dc} is decided by (27), as shown in Fig. 7(a).

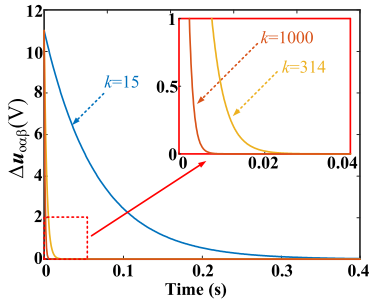

Fig. 8. VABOB's response after a grid voltage sag.

In Fig. 7(b), at the SF component, the VABOB only provides the virtual inductance, without an extra VR.

D. Dynamic-State Error Analysis

The previous analysis is based on the steady-state ideal grid situations, and the dc and the SF components are analyzed. In the next analysis, the dynamic-state nonideal grid situations, such as the voltage sag and frequency deviation, are analyzed.

Solving (20), the VABOB's time-domain solution is as follows:

$$\Delta \boldsymbol{x}=e^{-kt}\Delta \boldsymbol{x}\left(0\right) \tag{29}$$

where $\Delta \boldsymbol{x}\left(0\right)$ is the initial disturbance.

When the grid voltage is decreased by 0.1 p.u., the VABOB's response is shown in Fig. 8. The initial error is 11 V_{rms}. When k is 15, the convergence time is 0.33 s, time can be further reduced to 0.015 and 0.005 s with $k = 314$ and $k = 1000$, respectively. The convergence can refer to the 5τ principles of the exponential decay function. When the response time is longer than $5/k$, the error is smaller than 0.67% . This can also be explained as, if we increase k, the time constant $1/k$ is decreased. Therefore, the higher k is better for increasing the response speed.

If the grid frequency changes, the observer may have an observation error due to the assumption of $s = j\omega_n$. If it substitutes $s = j\omega$ in (26), then take the real part and the imaginary part as R' and L':

$$R'=\frac{R_g\left(k^2+\omega\omega_n\right)+k\left(L_g\omega+L_v\omega_n\right)\left(\omega_n-\omega\right)}{k^2+\omega_n^2}$$
$$L'=\frac{kR_g\left(\omega-\omega_n\right)+\left(L_g\omega+L_v\omega_n\right)\left(k^2+\omega\omega_n\right)}{k^2+\omega_n^2}. \tag{30}$$

The derivatives of k are as follows:

$$\frac{dR'}{dk}=\left(\omega_n-\omega\right)\frac{2R_gk\omega_n+\left(L_g\omega+L_v\omega_n\right)\left(\omega_n^2-k^2\right)}{\left(k^2+\omega_n^2\right)^2}$$
$$\frac{dL'}{dk}=\left(\omega_n-\omega\right)\frac{2k\omega_n\left(L_g\omega+L_v\omega_n\right)-R_g\left(\omega_n^2-k^2\right)}{\left(k^2+\omega_n^2\right)^2}. \tag{31}$$

The derivatives show the change rate of R' and L', which can contribute to the selection of k. The discussion takes the $\omega_n > \omega$ as an example. The denominator is k^4, and the numerator is k^2; therefore, a higher k can reduce the error. However, the special point is $k = \omega_n$, when k is equal to ω_n, $\omega_n{}^2$–$k^2 = 0$. When k is

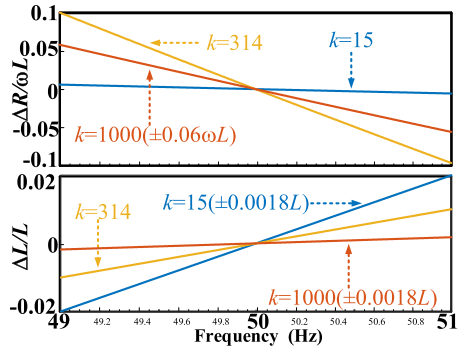

Fig. 9. VABOB's frequency response.

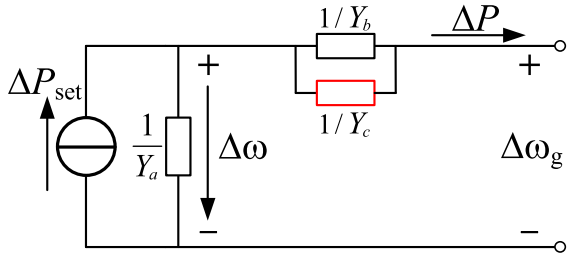

Fig. 10. P/ω admittance model of the VSG.

smaller than ω_{n}, the dominant value may be the R_{g}, L_{g}, or L_{v}. When k is larger than ω_{n}, the dominant value is k. Considering the extreme value of k^2/k^4 is 0 when k is infinite, k is better larger than ω_{n}.

Fig. 9 shows the frequency response results. The $\Delta R = R' - R$ and $\Delta L = L' - L$ are defined to depict the error. The ΔR shows that $k = 314$ gets a higher error than $k = 15$ or $k = 1000$. However, this value is small (as compared to the $X' = \omega L'$), and thus can be neglected. The ΔL is also small ($\pm 0.02L$ while $\Delta\omega_{\mathrm{g}}$ is between ± 1 Hz, $k = 15$). The ΔL can even be limited to $\pm 0.0018L$ when k is 1000. Thus, the error caused by the frequency deviation is ignored in the next discussions about the R/X ratio.

IV. VSG's Stability Analysis

In this section, the APCL's stability, including against the grid frequency deviation, is studied through the P/ω model. The transient SFR is derived and suppressed by the VABOB. Furthermore, the stability against the transient SFR when the grid voltage is sagged is verified through the phase portrait.

A. APCL Analysis Considering the Coupling

To test the influences of the VSG's stability, the open-loop gain $G_{POL}(s)$ of APCL, considering the power-coupling, is as follows:

$$G_{POL}(s) = G_P(s)\left[K_1(s) - \frac{K_2(s)K_3(s)G_Q(s)}{1 + K_4(s)G_Q(s)}\right]/s. \tag{32}$$

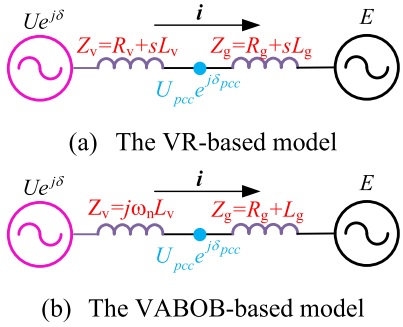

Fig. 11. VSG models used in the transient analysis. (a) VR-based model. (b) VABOB-based model.

However, this transfer function is abstract and not so easy to understand. Therefore, a P/ω admittance model shown in Fig. 10 is introduced to help illustrate the VSG's model [33].

The admittances of Y_{a}, Y_{b}, and Y_{c} are as follows:

$$Y_a = J\omega_{\mathrm{n}}s + D_{\mathrm{p}}$$

$$Y_b = \frac{K_1(s)}{s}$$

$$Y_c = -\frac{K_2(s)K_3(s)G_Q(s)}{s[1 + K_4(s)G_Q(s)]} = \frac{K_2(s)K_3(s)K}{\omega^2K^2 + (D_{\mathrm{q}} + K_4(s))^2} + j\frac{(D_{\mathrm{q}} + K_4(s))K_2(s)K_3(s)}{\omega^3K^2 + \omega(D_{\mathrm{q}} + K_4(s))^2}. \tag{33}$$

In (33), the $K_2(s) > 0$, but if $\delta_0 < \arctan(R/X)$, then the $K_3(s) < 0$, therefore, Y_{c} will contain the negative real part, and the negative conductance is introduced [34]. In the steady state, the VABOB does not contain the extra resistor; thus, it does not introduce extra negative torque. On the contrary, VABOB can alleviate the negative torque caused by the high R/X:

$$\frac{R_{\mathrm{g}}}{\omega(L_{\mathrm{v}} + L_{\mathrm{g}})} < \frac{R_{\mathrm{g}}}{\omega L_{\mathrm{g}}}. \tag{34}$$

When the grid frequency is changed, the impedance under the VABOB can be treated as equal to the real impedance. Therefore, the VABOB can enhance the APCL stability, as inductive virtual impedance reduces the R/X ratio.

B. Transient SFR Analysis

The VSG models used in the transient SFR and stability analysis are shown in Fig. 11. One more intermediate variable $U_{\mathrm{pcc}}e^{j\delta_{\mathrm{pcc}}}$ is used to calculate the VSG's output power.

When the VR-based method is applied, the circuit obeys

$$U_{\mathrm{pcc}}e^{\mathrm{j}\delta\mathrm{pcc}} = \frac{Z_{\mathrm{g}}Ue^{j\delta} + Z_{\mathrm{v}}E}{Z_{\mathrm{v}} + Z_{\mathrm{g}}}$$

$$i = \frac{Ue^{j\delta} - U_{\mathrm{pcc}}e^{\mathrm{j}\delta\mathrm{pcc}}}{Z_{\mathrm{v}}} = \frac{Ue^{j\delta} - E}{Z_{\mathrm{v}} + Z_{\mathrm{g}}}. \tag{35}$$

At the 0_+ moment of grid voltage sag, the VSG remains stable. Thus, to keep the voltage deviation ΔE, the fault current $\Delta \boldsymbol{i}(0_+)$

TABLE I
SELECTION OF k

Constraint	Requirement for k
Overall Constraint	Maximum 1/10 f_s
Grid Voltage Sag (Section III)	Higher k is better
Frequency Deviation (Section III)	Higher k than ω_n
Steady-State SFR (Section III)	Higher k is better
Transient SFR (Section IV)	Higher k is better
Final k	k = 1/10 f_s = 1000

TABLE II
EXPERIMENTAL PARAMETERS

Parameters	Value	Parameters	Value
Apparent power S_{set}	2 kVA	Rotational inertia J	0.057
Active power P_{set}	1 p.u.	Integrator gain K	7.1
Filter inductance L_f	2.5 mH	Damping ratio D_p	5
Filter capacitance C_g	2.2 μF	Q-V coefficient D_q	64.2
Grid inductance L_g	1 mH	Grid voltage E_m	155.6 V
Grid resistance R_g	0.05 Ω	Sampling Period 1/f_s	100 μs

should increase

$$\begin{aligned} U\angle\delta\left(0_+\right) &= U\angle\delta\left(0_-\right) \\ E\left(0_+\right) &= E\left(0_-\right) - \Delta E \\ \boldsymbol{i}\left(0_+\right) &= \boldsymbol{i}\left(0_-\right) + \Delta\boldsymbol{i}\left(0_+\right) \end{aligned} \tag{36}$$

where the (0_+) and (0_-) mean the corresponding values before and after and grid voltage sag moment. ΔE and $\Delta\,\boldsymbol{i}\,(0_+)$ mean the grid voltage sag value and the transient fault current.

The formulas above imply that the transient behavior can be divided into two parts: the steady-state current part $\boldsymbol{i}\,(0_-)$ and the transient fault current part $\Delta\,\boldsymbol{i}\,(0_+)$. By substituting (36) into (35), these currents can be obtained as follows:

$$\begin{aligned} \boldsymbol{i}\left(0_-\right) &= \frac{Ue^{j\delta}\left(0_-\right) - E\left(0_-\right)}{Z_v + Z_g} \\ \Delta\boldsymbol{i}\left(0_+\right) &= \frac{\mathcal{L}\left[\Delta E e^{j\omega_n t}\right]}{R + sL} \end{aligned} \tag{37}$$

where $\mathcal{L}$ is the Laplace transformation.

This is, $\Delta\,\boldsymbol{i}\,(0_+)$ is excited by the grid voltage sag vector $\Delta E e^{j\omega_n t}$. The time-domain solution for it is as follows:

$$\begin{aligned} \Delta i\left(0_+\right) &= \frac{\Delta E}{R + j\omega_n L}\left(e^{j\omega_n t} - e^{-\mu t}\right) \\ \mu &= \frac{R}{L}. \end{aligned} \tag{38}$$

It contains the steady-state and the transient components. The transient component is a decreasing dc function, and therefore, the transient SFR occurs. Besides, the convergence time of the transient SFR is decided by the $\mu = R/L$, a higher R or lower L can reduce this time.

To solve the conflict, the convergence equation under the VABOB is derived. First, when the grid voltage sag occurs, the VABOB should track this value. Based on the time-domain convergence (29), the frequency-domain equation for the $\Delta E e^{j\omega_n t}$ is as follows:

$$\Delta E\left(s\right) = \mathcal{L}\left[\Delta E e^{j\omega_n t}\left(1 - e^{-kt}\right)\right]. \tag{39}$$

TABLE III
COMPARISON SETTINGS

No.	Method	Impedance	Deviations
(a)	DOB-VI	R_v = 0.5 Ω	P_{set} 0->1 p.u.
(b)		L_v = 7.5 mH	$\Delta\omega_g$ = −0.1 Hz
(c)		$\lvert Z_v\rvert$ = 2.41 Ω	ΔE = −0.1 p.u.
(d)	VABOB	R_v = 0.0 Ω	P_{set} 0->1 p.u.
(e)		L_v = 7.5 mH	$\Delta\omega_g$ = −0.1 Hz
(f)		$\lvert Z_v\rvert$ = 2.36 Ω	ΔE = −0.1 p.u.
(g)	DOB-VI	R_v = 2.24 Ω	P_{set} 0->1 p.u.
(h)		L_v = 7.5 mH	$\Delta\omega_g$ = −0.1 Hz
(i)		$\lvert Z_v\rvert$ = 3.25 Ω	ΔE = −0.1 p.u.
(j)	VABOB	R_v = 0.0 Ω	P_{set} 0->1 p.u.
(k)		L_v = 10.4 mH	$\Delta\omega_g$ = −0.1 Hz
(l)		$\lvert Z_v\rvert$ = 3.25 Ω	ΔE = −0.1 p.u.

Then, according to Fig. 11(b), the impedance from the VSG to the grid is $j\omega_n L_v + Z_g$; thus, the relationship between the observed current and the $\Delta E(s)$ is as follows:

$$\begin{aligned} \Delta i\left(0_+\right) &= \frac{\Delta E\left(s\right)}{j\omega_n L_v + Z_g} \\ \Delta E\left(s\right) &= \left(\frac{1}{s - j\omega_n} - \frac{1}{s + k - j\omega_n}\right)\Delta E. \end{aligned} \tag{40}$$

The time-domain solution is as follows:

$$\begin{aligned} \frac{\Delta i\left(0_+\right)}{\Delta E} &= D_1 e^{j\omega_n t} + D_2 e^{-kt} e^{j\omega_n t} - D_1 D_2 k L_g e^{-\frac{R_g}{L_g}t} e^{j\omega_n \frac{L_v}{L_g}t} \\ D_1 &= \frac{1}{R_g + j\omega_n L} \\ D_2 &= \frac{1}{kL_g - R_g - j\omega_n L}. \end{aligned} \tag{41}$$

It shows that the VABOB does not contain the dc function component. Instead, it includes a steady-state and two transient components. Thus, the transient SFR is suppressed.

The influence of the two transient components is studied. It has two different convergence time constants and frequencies. The second item indicates a fixed frequency component at ω_n, and the time constant is $1/k$. Thus, it requires a higher k for faster convergence time. The third item indicates a variable frequency component at $\omega_n * L_v/L_g$, and the time constant τ is L_g/R_g. Although the τ is uncontrollable, the frequency is controllable. The frequency components of power caused by the third item are $(1-L_v/L_g)\omega_n$ and $(1+L_v/L_g)\omega_n$. As the $G_P(s)$ and the $G_Q(s)$ are LPFs, the L_v/L_g is better larger than 3 to ensure the lowest power component is larger than the $2\,\omega_n$, thus they are filtered [6].

C. Transient Stability Analysis

After the fault current transient behavior, the APCL and the RPCL start to regulate the deviation of P_e and Q_e, respectively. The VSG's state space equation can be defined as follows:

$$\begin{bmatrix} \dot{\delta} \\ \Delta\dot{\omega} \\ \dot{U} \end{bmatrix} = \begin{bmatrix} \Delta\omega \\ \frac{P_{set}}{J\omega_n} - \frac{P_e}{J\omega_n} - \frac{D_p}{J}\Delta\omega \\ Q_{set} - Q_e + D_q\left(U_n - U_{pcc}\right) \end{bmatrix}. \tag{42}$$

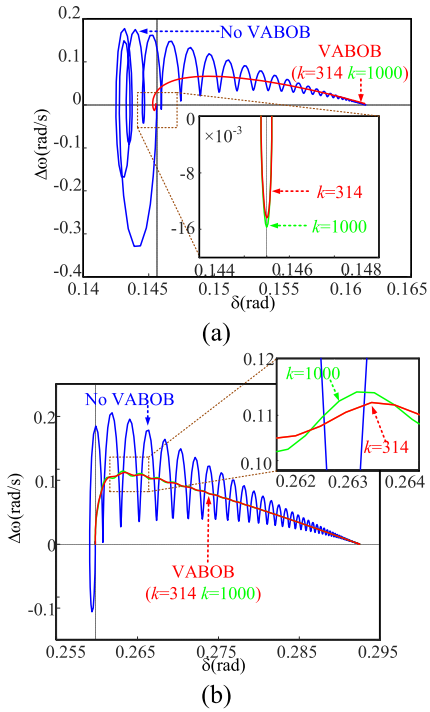

Fig. 12. Phase portrait of VSG under grid voltage sag. (a) $L_{\mathrm{g}} = 1$ mH. (b) $L_{\mathrm{g}} = 7.5$ mH.

The P_{e} and Q_{e} are the real part and the imaginary part of the PCC power $\boldsymbol{U}_{\mathrm{pcc}}\angle\delta_{\mathrm{pcc}} * \boldsymbol{i}$, while the PCC voltage is as follows:

$$U_{\mathrm{pcc}} e^{j\delta_{\mathrm{pcc}}}(0_+) = i(0_+) Z_{\mathrm{g}} + E(0_+). \tag{43}$$

The initial conditions are set to δ_0, 0, and U_0, respectively. Thus, the phase portraits in Fig. 12 can be drawn. When no VABOB is used, there is a decreasing periodic disturbance on the power angle, verifying the transient component of (38). When the VABOB is used, the transient SFR modal is removed, corresponding to the no dc function in solution (41). When L_{g} is increased from 1 to 7.5 mH, there is a small periodic disturbance laid on the power angle convergence path, verifying that the low ratio of $L_{\mathrm{v}}/L_{\mathrm{g}}$ may cause the third item not to be fully filtered by the $G_P(s)$ and the $G_Q(s)$.

D. Selection of k

The selection of k is summarized in Table I. First of all, considering the harmonic filtering effect, the maximum k is limited to not more than $1/10\, f_{\mathrm{s}}$. Then, to improve the VSG's performance against the steady-state SFR, transient SFR, and the grid voltage sag, a higher k is better. The special one is the grid frequency deviation; the VABOB requires a larger k than ω_{n}. Therefore, k is selected as $1/10\, f_{\mathrm{s}} = 1000$.

V. Simulation And Experiment Verification

Simulation and experimental studies are carried out to validate the effectiveness of the proposed method. The setup is shown in Fig. 13, the controller is RTU-BOX 205 with core processor TMS320C28346. The VSG algorithm is calculated in the processor and outputs the power from the inverter to the grid. The inverter and the filter are RTI-INV8040IR and RTF-LC25, respectively. This powers the ability at 40Arms output current, 560Vrms ac voltage, and 800 V dc voltage. The ac grid is achieved by the inductor series with the grid simulator Chroma 61815, which supports a maximum 15 kVA operation. Thus,

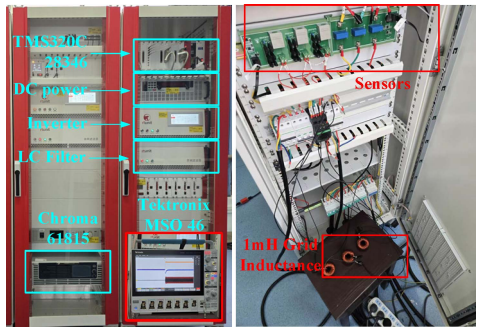

Fig. 13. Experiment setup.

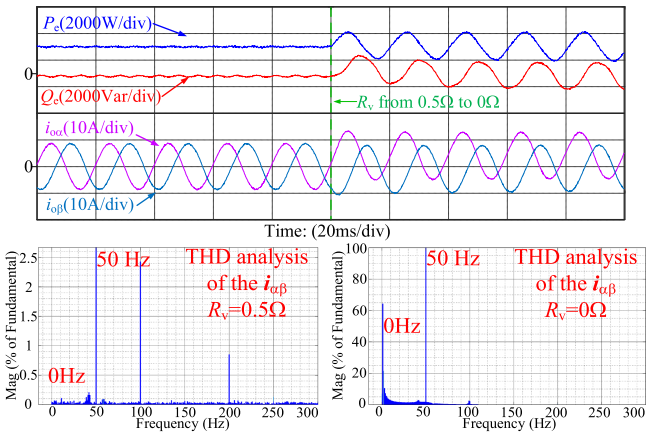

Fig. 14. Steady-state SFR phenomenon verification.

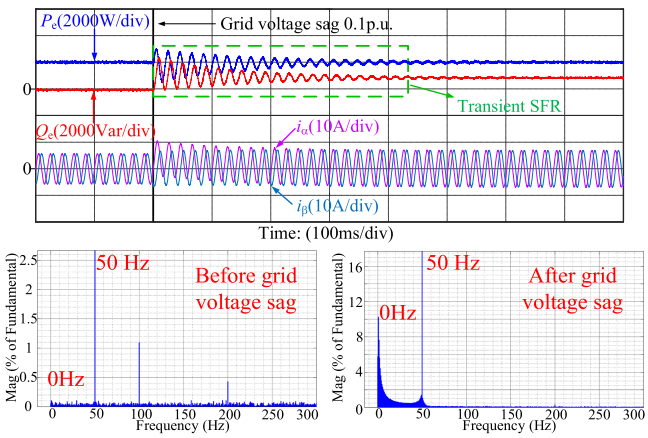

Fig. 15. Transient SFR phenomenon verification.

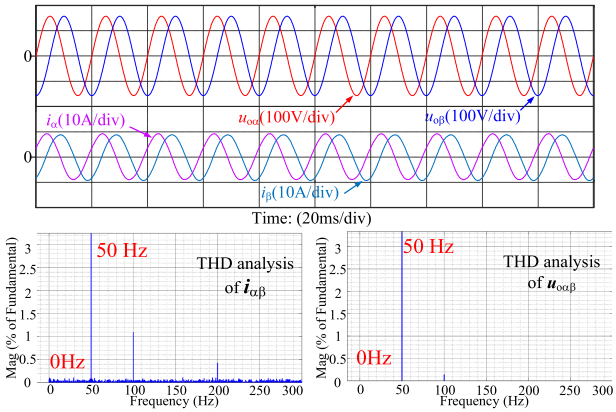

Fig. 16. Steady-state SFR suppression of the VABOB.

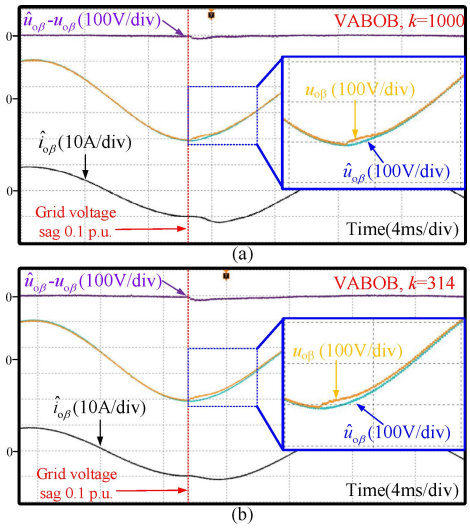

Fig. 17. VABOB's performance under grid voltage sag. (a) $k = 1000$. (b) $k = 314$.

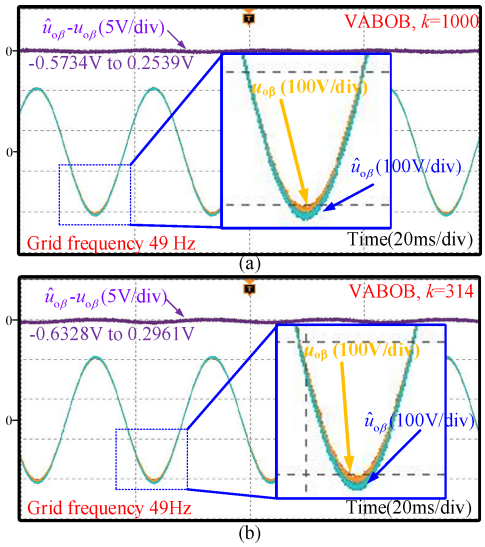

Fig. 18. VABOB's performance under a grid frequency drop. (a) $k = 1000$. (b) $k = 314$.

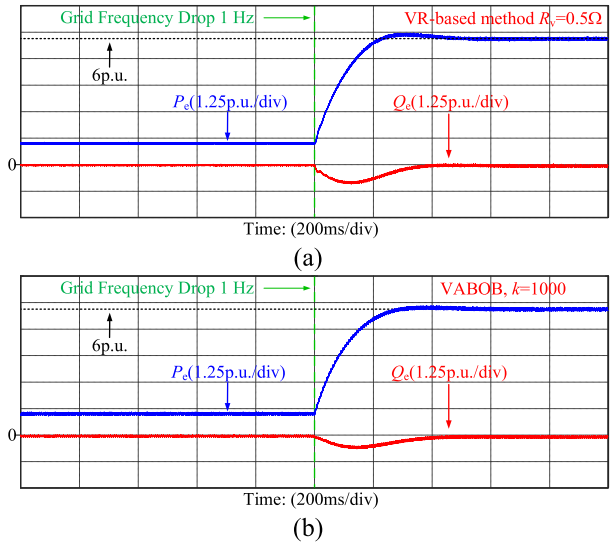

Fig. 19. Dynamic-state response when the grid frequency is dropped by 1 Hz. (a) VR-based method with R_v is 0.5 Ω. (b) VABOB method with $k = 1000$.

the short-circuit ratio of the experiments is 15/2 = 7.5. The oscilloscope is a Tektronix MSO 46.

The simulation parameters are the same as the experimental ones shown in Table II. The arrangement of the simulation and experiment is as follows.

1) In Section V-A, based on the simulation, the existence of steady-state and the transient SFR are verified, and the steady-state SFR is suppressed based on the VABOB.
2) In Section V-B, the dynamic performance of VABOB is verified through both simulations and experiments, including the grid frequency deviation, grid voltage sag, and different k.
3) In Section V-C, comparative experiments between the DOB-VI and the VABOB, including the P_{set} change, the grid frequency drop, and the grid voltage sag, are conducted.

A. SFR and Suppression Strategy Validation

To verify the existence of the steady-state, transient SFR, and the effectiveness of the VABOB, simulations are conducted in this section.

First, the steady-state SFR phenomenon is verified, and a VR switch simulation result is shown in Fig. 14. When R_{v} is 0.5 Ω, the system can stay stable, because the system's resistance is compensated by the R_{v}. However, after the R_{v} is reduced from 0.5 to 0 Ω, the $1/\mu$ is reduced to $L/R = 0.0085/0.05 = 0.17$ s, which is larger than the τ of the RPCL: $K/D_{\text{q}} = 7.1/64.2 = 0.11$ s. Thus, the power starts to oscillate around 50 Hz. The THD analysis also shows that the dc component is increased from almost 0 to 64.7% when R_{v} is reduced to 0 Ω.

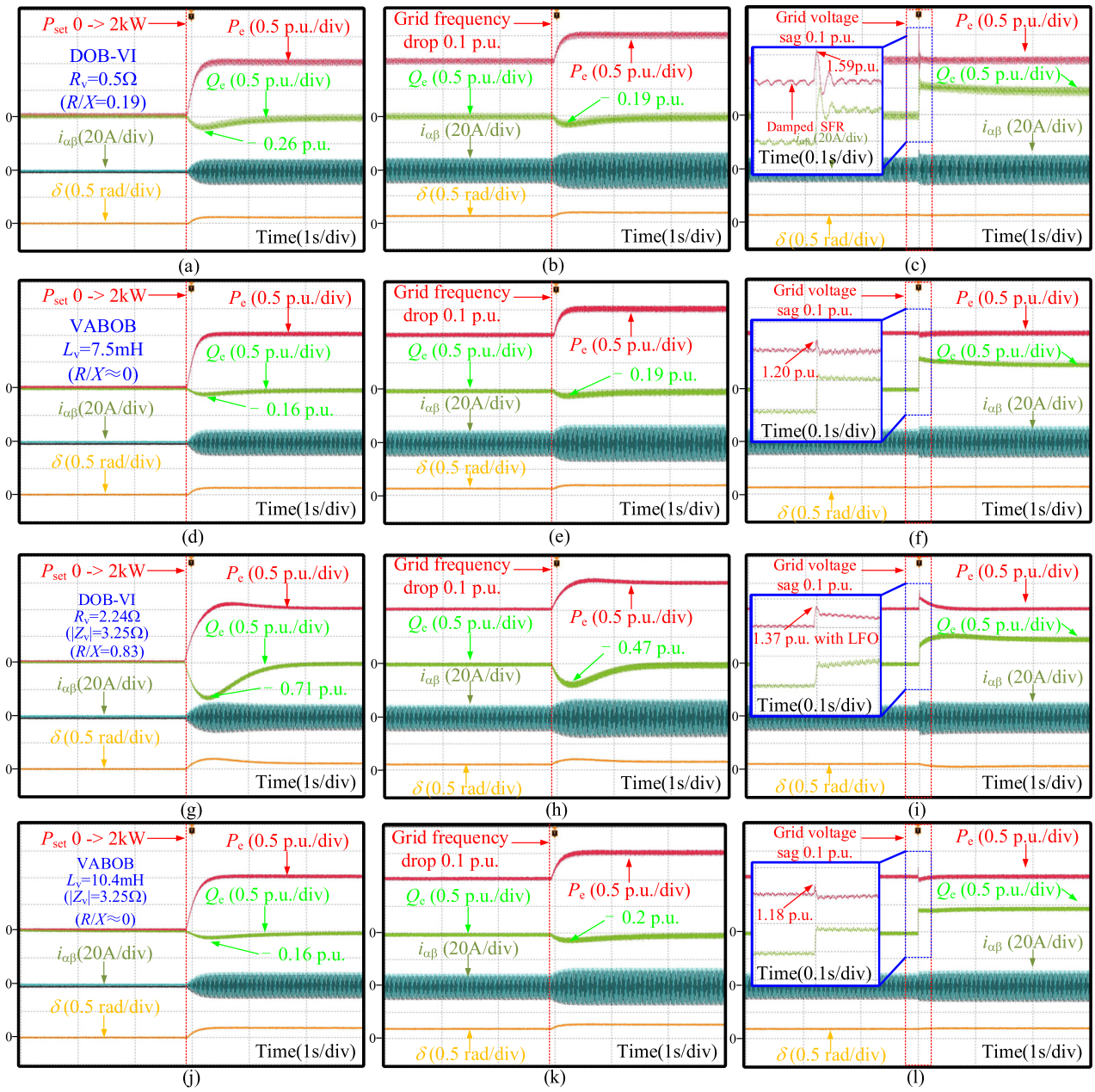

Fig. 20. The dynamic-state performance verification. (a), (b), and (c): DOB-VI method with $R_{\mathrm{v}} = 0.5\ \Omega$, under the Pset from 0 to 1 p.u., the grid frequency drop of 0.1 Hz, and the grid voltage sag of 0.1 p.u., respectively. (d), (e), and (f): VABOB method with $L_{\mathrm{v}} = 7.5$ mH, under the Pset from 0 to 1 p.u., the grid frequency drop of 0.1 Hz, and the grid voltage sag of 0.1 p.u., respectively. (g), (h), and (i): DOB-VI method with $R_{\mathrm{v}} = 2.24\ \Omega$, under the Pset from 0 to 1 p.u., the grid frequency drop of 0.1 Hz, and the grid voltage sag of 0.1 p.u., respectively. (j), (k), and (l): VABOB method with $L_{\mathrm{v}} = 10.4$ mH, under the Pset from 0 to 1 p.u., the grid frequency drop of 0.1 Hz, and the grid voltage sag of 0.1 p.u., respectively.

Then, to verify the transient SFR, the R_{g} is increased to 0.1 Ω to ensure the steady-state SFR is suppressed, and R_{v} is set to 0 Ω. It is noteworthy that these values of R are idealized only for the transient SFR verification. The results are shown in Fig. 15. When the grid voltage is sagged by 0.1 p.u., the transient SFR occurs. The results also corresponded to the (38) and Fig. 12. The $1/\mu$ is $L/R = 0.0085/0.1 = 0.085$ s, now it is smaller than the τ value of the RPCL; thus, the convergence time of the transient component is $5{*}0.085 = 0.425$ s. The THD analysis after the grid voltage sag shows a 10.3% percentage at the dc component, which also verifies the transient SFR.

To verify the steady-state SFR suppression effect of the VABOB, the R_{g} is set back to 0.05 Ω. The VSG's output current $\boldsymbol{i}_{\alpha\beta}$, the output voltage $\boldsymbol{u}_{o\alpha\beta}$, and the corresponding THD analysis are shown in Fig. 16. Although the R_{v} is set to 0, the THD analysis shows that the dc percentage is low. Therefore, the steady-state SFR is suppressed by the VABOB.

B. VABOB Verification

To further verify the effectiveness of the VABOB, the experiments are conducted, including the grid frequency drop, the grid voltage sag, and with different k. The grid voltage drop experiment is to study the influence of k on the convergence of the VABOB. And the grid frequency deviation experiment is to study the observation error under the $\omega_g \neq \omega_n$.

In Fig. 17, when the grid voltage is sagged by 0.1 p.u., it can be seen that the observed voltage has an error at 0_+ time, as compared to the real PCC voltage. However, the error can be converged to 0, and the time constant is $1/k$ according to (29). When $k = 1000$ in Fig. 17(a), its convergence is faster than that when k 314 in Fig. 17(b). Thus, for the faster convergence time under the grid voltage sag, a higher k is reasonable.

Then, the grid frequency is set to 49 Hz. The results are shown in Fig. 18(a), when $k = 1000$, the observation error is –0.5734 to 0.2539 V; in comparison, the VABOB has a larger observer error at –0.6328 to 0.2961 V when $k = 314$ in Fig. 18(b). Thus, a larger k can reduce the observer error under the grid frequency deviation situation. The error can be explained by the extra small resistor and inductance, as shown in Fig. 9.

The simulation results in Fig. 19 also verify that the extra R/X ratio caused by the VABOB is small. When the grid frequency is dropped by 1 Hz, the VSG should increase the active power by 5 p.u.; thus, the final target is 6 p.u. However, the VR-based method shows power overshoot in Fig. 19(a), corresponding to the higher R/X. As a comparison, the VABOB does not have the active power overshoot in Fig. 19(b); thus, the stability against the grid frequency deviation is verified. Further experimental validation of the influence of the grid frequency drop is shown in the next subsection.

C. Dynamic-State Performance

In the dynamic-state performance experiments, the P_{set} from 0 to 1 p.u., the grid frequency drop of 0.1 Hz, and the grid voltage sag of 0.1 p.u. are conducted. The methods are the VABOB and the DOB-VI [27], with the same bandwidth k (or ω_c of the DOB-VI) at $1/10 f_s = 1000$.

The comparison settings are shown in Table III. The DOB-VI method with 0.5 and 2.44 Ω R_v is conducted, where 0.5 Ω R_v is to ensure that the steady-state SFR is damped, and 2.44 Ω R_v is to further damp the transient SFR. The L_v of the VABOB is 7.5 and 10.4 mH, for keeping the same $|Z_v|$ with the DOB-VI method.

The results are shown in Fig. 20. When the R_v is 0.5 Ω, the $R/X = 0.19$; thus, when the P_{set} is increased or the grid frequency is dropped, the LFO does not appear, as shown in Fig. 20(a) and (b). However, the R_v reduces the positive torque; therefore, the Q_e response is deteriorated due to the power coupling from the APCL. The VABOB's corresponding Q_e response comparison is shown in Fig. 20(d) and (e). Besides, in Fig. 20(c), when the grid voltage is sagged, it can be seen that the periodic power oscillation and the P_e overshoot at 0.59 p.u., before and after the grid voltage sag, respectively. As a comparison, the VABOB does not contain the steady-state or the transient SFR in Fig. 20(f).

Then, the R_v of the DOB-VI is increased to 2.24 Ω; this value corresponds to the $|R_{dc}|$ of the VABOB, as analyzed in Fig. 6. Then, the L_v of the VABOB is increased to 10.4 mH to ensure the consistency of $|Z_v|$ with DOB-VI. When the R_v is increased, although the steady-state and the transient SFR are well damped in Fig. 20(i). The high negative torque is introduced; thus, the LFO appears in both Fig. 20(g) and (h), with a $|Q_e|$ overshoot larger than 0.5 p.u. As a comparison, the VABOB can still keep the APCL's stability in Fig. 20(j) and (k). What's more, when the VABOB is used, the P_e spike in a short term (about 5 ms $= 5/k$) from Fig. 20(f) and (l) also verifies the transient item of (41).

VI. Conclusion

The small-signal model and the transient analysis of the VSG show that the VR is useful for steady-state and transient SFR suppression. But the VR at the SF decreases the VSG's dynamic stability, as shown through the P/ω model and the VSG's phase portrait. The VABOB has been designed for enhanced dynamic response performance. It represents the high resistance for the steady-state and transient SFR, and no extra VR at the SF. Moreover, the VABOB's performance with grid voltage and frequency deviations is analyzed, which shows the fast convergence speed under voltage deviation and negligible error under frequency deviation situations. To verify the validity of the VABOB, both simulation and experimental studies are conducted. The results show that the VABOB can eliminate the SFR and reduce the maximum by 0.39 p.u. power overshoot when the grid voltage is sagged by 0.1 p.u., as compared to the VR-based method with $R/X = 0.19$. By 0.55 p.u. reactive power overshoot reduction when power given is increased from 0 to 1 p.u., as compared to the VR-based method with $R/X = 0.83$. The result verifies that the VABOB can suppress the SFR and enhance the dynamic response performance by decreasing R/X.

References

[1] X. Wu et al., "Grid-forming control and experimental validation for high voltage transformerless battery energy storage system," *IEEE Trans. Power Electron.*, vol. 40, no. 4, pp. 4889–4901, Apr. 2025, doi: 10.1109/TPEL.2024.3510361.

[2] T. Xu, S. Jiang, Y. Zhu, and G. Konstantinou, "Composite power-frequency synchronization loop for enhanced frequency response considering current and power limits of grid-forming converters," *IEEE Trans. Power Electron.*, vol. 40, no. 4, pp. 4969–4983, Apr. 2025, doi: 10.1109/TPEL.2024.3512592.

[3] H. Zhang, W. Xiang, and J. Wen, "Dual grid-forming control with energy regulation capability of MMC-HVDC system integrating offshore wind farms and weak grids," *IEEE Trans. Power Syst.*, vol. 39, no. 1, pp. 261–272, Jan. 2024, doi: 10.1109/TPWRS.2023.3244807.

[4] H. Xu, X. Zhang, F. Liu, R. Shi, C. Yu, and R. Cao, "A reactive power sharing strategy of VSG based on virtual capacitor algorithm," *IEEE Trans. Ind. Electron.*, vol. 64, no. 9, pp. 7520–7531, Sep. 2017, doi: 10.1109/TIE.2017.2686374.

[5] F. Li and J. Ma, "Stability studies of grid-forming and grid-following inverter penetrated systems with different external power system models," *IEEE Trans. Power Del.*, vol. 39, no. 5, pp. 2580–2591, Oct. 2024, doi: 10.1109/TPWRD.2024.3407110.

[6] H. Wu et al., "Small-signal modeling and parameters design for virtual synchronous generators," *IEEE Trans. Ind. Electron.*, vol. 63, no. 7, pp. 4292–4303, Jul. 2016, doi: 10.1109/TIE.2016.2543181.

[7] J. Wang and K. Ma, "Inertia and grid impedance emulation of power grid for stability test of grid-forming converter," *IEEE Trans. Power Electron.*, vol. 38, no. 2, pp. 2469–2480, Feb. 2023, doi: 10.1109/TPEL.2022.3210926.
[8] Y. Yu, M. Zhang, M. Antoine, and H. Li, "Analysis of synchronous frequency resonance in VSG based on the sequence impedance models," in *Proc. 22nd Int. Conf. Elect. Mach. Syst.*, 2019, pp. 1–6, doi: 10.1109/ICEMS. 2019.8922440.
[9] X. Zhou, S. Cheng, X. Wu, and X. Rao, "Influence of photovoltaic power plants based on VSG technology on low frequency oscillation of multi-machine power systems," *IEEE Trans. Power Del.*, vol. 37, no. 6, pp. 5376–5384, Dec. 2022, doi: 10.1109/TPWRD.2022. 3177042.
[10] Y. Wang et al., "Low-frequency oscillation in power grids with virtual synchronous generators: A comprehensive review," *Renewable Sustain. Energy Rev.*, vol. 207, 2025, Art. no. 114921, doi: 10.1016/j.rser. 2024.114921.
[11] G. Li, Y. Shao, X. Liu, and J. Chen, "A virtual series compensation control of virtual synchronous generator for improving energy transmission efficiency," *IEEE Trans. Emerg. Sel. Topics Power Electron.*, vol. 13, no. 2, pp. 2442–2452, Apr. 2025, doi: 10.1109/JESTPE.2024.3519575.
[12] J. Guo et al., "Impedance analysis and stabilization of virtual synchronous generators with different DC-link voltage controllers under weak grid," *IEEE Trans. Power Electron.*, vol. 36, no. 10, pp. 11397–11408, Oct. 2021, doi: 10.1109/TPEL.2021.3070038.
[13] X. Wang, Y. W. Li, F. Blaabjerg, and P. C. Loh, "Virtual-impedance-based control for voltage-source and current-source converters," *IEEE Trans. Power Electron.*, vol. 30, no. 12, pp. 7019–7037, Dec. 2015, doi: 10.1109/TPEL.2014.2382565.
[14] M. Li et al., "Analysis and improvement of large-disturbance stability for grid-connected VSG based on output impedance optimization," *IEEE Trans. Power Electron.*, vol. 37, no. 8, pp. 9807–9826, Aug. 2022, doi: 10.1109/TPEL.2022.3153563.
[15] B. Long, S. Zhu, J. Rodriguez, J. M. Guerrero, and K. T. Chong, "Enhancement of power decoupling for virtual synchronous generator: A virtual inductor and virtual capacitor approach," *IEEE Trans. Ind. Electron.*, vol. 70, no. 7, pp. 6830–6843, Jul. 2023, doi: 10.1109/TIE. 2022.3206701.
[16] H. Wang et al., "Admittance-based stability analysis of current-controlled VSG considering the frequency coupling characteristics," *IEEE Trans. Emerg. Sel. Topics Power Electron.*, vol. 11, no. 1, pp. 1191–1202, Feb. 2023, doi: 10.1109/JESTPE.2022.3213258.
[17] J. D. V. Leon, A. Tarraso, J. I. Candela, J. Rocabert, and P. Rodriguez, "Grid-forming controller based on virtual admittance for power converters working in weak grids," *IEEE Trans. Emerg. Sel. Topics Power Electron.*, vol. 4, no. 3, pp. 791–801, Jul. 2023, doi: 10.1109/JESTIE.2023. 3244744.
[18] C. Busada, S. Gomez Jorge, and J. A. Solsona, "Current-controlled synchronverter: A grid fault tolerant grid forming inverter," *IEEE Trans. Ind. Electron.*, vol. 71, no. 4, pp. 3233–3241, Apr. 2024, doi: 10.1109/TIE.2023.3277109.
[19] K. M. Alawasa and Y. A.-R. I. Mohamed, "A simple approach to damp SSFR in series-compensated systems via reshaping the output admittance of a nearby VSC-based system," *IEEE Trans. Ind. Electron.*, vol. 62, no. 5, pp. 2673–2682, May 2015, doi: 10.1109/TIE.2014.2363622.
[20] D. Zhu, X. Li, S. Zhou, X. Zhong, X. Zou, and Y. Kang, "Optimized power decoupling control for grid-forming converter under different R/X ratios of grid impedance," *IEEE Trans. Circuits Syst. II, Express Briefs*, vol. 72, no. 12, pp. 2052–2056, Dec. 2025, doi: 10.1109 /TCSII.2025.3599886.
[21] X. Xiong, C. Wu, and F. Blaabjerg, "Effects of virtual resistance on transient stability of virtual synchronous generators under grid voltage sag," *IEEE Trans. Ind. Electron.*, vol. 69, no. 5, pp. 4754–4764, May 2022, doi: 10.1109/TIE.2021.3082055.
[22] N. Mohammed, M. H. Ravanji, W. Zhou, and B. Bahrani, "Online grid impedance estimation-based adaptive control of virtual synchronous generators considering strong and weak grid conditions," *IEEE Trans. Sustain. Energy*, vol. 14, no. 1, pp. 673–687, Jan. 2023.
[23] S. Chen, Y. Sun, H. Han, S. Fu, S. Luo, and G. Shi, "A modified VSG control scheme with virtual resistance to enhance both small-signal stability and transient synchronization stability," *IEEE Trans. Power Electron.*, vol. 38, no. 5, pp. 6005–6014, May 2023, doi: 10.1109/TPEL.2023.3243025.
[24] X. Xiong, Y. Zhou, B. Luo, P. Cheng, and F. Blaabjerg, "Analysis and suppression strategy of synchronous frequency resonance for grid-connected inverters with power-synchronous control method," *IEEE Trans. Power Electron.*, vol. 38, no. 6, pp. 6945–6955, Jun. 2023.
[25] N. Dong, M. Li, X. Chang, W. Zhang, H. Yang, and R. Zhao, "Robust power decoupling based on feedforward decoupling and extended State observers for virtual synchronous generator in weak grid," *IEEE Trans. Emerg. Sel. Topics Power Electron.*, vol. 11, no. 1, pp. 576–587, Feb. 2023, doi: 10.1109/JESTPE.2022.3207973.
[26] J. Yu, Y. Qi, H. Deng, X. Liu, and Y. Tang, "Evaluating small-signal synchronization stability of grid-forming converter: A geometrical approach," *IEEE Trans. Ind. Electron.*, vol. 69, no. 9, pp. 9087–9098, Sep. 2022, doi: 10.1109/TIE.2021.3113000.
[27] G. Heo, S. Choi, and Y. Park, "Disturbance-observer-based virtual impedance for virtual synchronous generators," *IEEE Trans. Ind. Appl.*, vol. 61, no. 6, pp. 8595–8605, Nov./Dec. 2025, doi: 10.1109/TIA.2025. 3573232.
[28] S. Wang, A. Jiang, J. Ma, P. Wang, R. Zhang, and T. Liu, "Transient stability analysis for hybrid parallel-connected converters by two-dimensional phase portrait," *IEEE Trans. Power Electron.*, vol. 40, no. 6, pp. 7765–7776, Jun. 2025, doi: 10.1109/TPEL.2025.3532938.
[29] D. Zhu, C. Zheng, Y. Yang, J. Hu, X. Zou, and Y. Kang, "Transient synchronization stability analysis and enhancement of DFIG-based wind turbines from perspective of power transmission balance," *IEEE Trans. Power Electron.*, vol. 41, no. 1, pp. 50–55, Jan. 2026, doi: 10.1109/TPEL.2025.3593482.
[30] X. Xia, X. Zhao, and J. Liang, "A novel control strategy to enhance the transient performance of grid-forming converters," *IEEE Trans. Ind. Electron.*, vol. 73, no. 1, pp. 779–790, Jan. 2026, doi: 10.1109/TIE.2025.3595969.
[31] L. Guo et al., "A virtual-flux State observer-based inductance identification method for model predictive control of grid-tied inverters with a finite phase angle set-based PLL," *IEEE Trans. Ind. Electron.*, vol. 70, no. 8, pp. 8009–8021, Aug. 2023.
[32] W. Xu et al., "Discrete space vector modulation-based MPCC with inductance identification for thrust ripple suppression in linear induction machine," *IEEE Trans. Power Electron.*, vol. 39, no. 10, pp. 12883–12893, Oct. 2024.
[33] B. Qin, Y. Xu, C. Yuan, and J. Jia, "A unified method of frequency oscillation characteristic analysis for multi-VSG grid-connected system," *IEEE Trans. Power Del.*, vol. 37, no. 1, pp. 279–289, Feb. 2022, doi: 10.1109/TPWRD.2021.3058208.
[34] M. Yang, Y. Wang, and J. M. Guerrero, "Impact of reactive power control on low-frequency oscillation of virtual synchronous generators," *IEEE Trans. Power Syst.*, vol. 40, no. 4, pp. 3604–3607, Jul. 2025, doi: 10.1109/TPWRS.2025.3567160.

Dongren Dai received the B.S. and M.S. degrees in building electricity and intelligence, and electrical engineering from the Zhengzhou University of Light Industry, Zhengzhou, China, in 2020 and 2023, respectively. He is currently working toward the Ph.D. degree in electrical engineering in Guangxi University, Nanning, China. His research interests include the stability of grid-forming inverters and predictive control.

Jinghua Li (Senior Member, IEEE) received the B.S. and M.S. degrees from North China Electric Power University, Beijing, China, in 2003 and 2006, respectively, and the Ph.D. degree from Guangxi University, Nanning, China, in 2011, all in power engineering. She was a Postdoctoral Researcher of electrical engineering with the Huazhong University of Science and Technology, Wuhan, China. She is currently a Professor and Ph.D. supervisor with the Department of Electrical Engineering, Guangxi University. Her main research interests include power system operation and planning, particularly in the application of optimization methods to power systems.

Fei Lan received the M.S. degree in electrical engineering from Guangxi University, Nanning, China, in 2006. He is currently a Professorate Senior engineer with the Department of Electrical Engineering, Guangxi University. His main research interests include power system operation and control.

Wei Tian (Member, IEEE) received the Ph.D. degree in electrical engineering from Hunan University, Changsha, China, in 2024. He is currently an Assistant Professor with the School of Electrical Engineering, Guangxi University, Nanning, China. His research interests include converter modeling and control, electroacoustic transducer systems, impedance matching networks, and wireless power transfer technology.